# Deciphering the hierarchical structure of phosphate glasses using persistent homology with optimized input radii

Xiao, Yongbao; Du, Tao; Sørensen, Søren Strandskov; Chen, Zhimin; Biscio, Christophe; Fajstrup, Lisbeth; Bauchy, Mathieu; Smedskjær, Morten Mattrup

*Published in:*
Physical Review Materials

*DOI (link to publication from Publisher):*
10.1103/PhysRevMaterials.7.065602

*Publication date:*
2023

*Document Version*
Accepted author manuscript, peer reviewed version

# Deciphering the hierarchical structure of phosphate glasses using persistent homology with optimized input radii

Yongbao Xiao[1,2], Tao Du[1,*], Søren S. Sørensen[1], Zhimin Chen[1], Christophe A.N. Biscio[3], Lisbeth Fajstrup[3], Mathieu Bauchy[4], Morten M. Smedskjaer[1,*]

[1]*Department of Chemistry and Bioscience, Aalborg University, Aalborg, 9220, Denmark*

[2]*School of Physics and Optoelectronics, State Key Laboratory of Luminescent Materials and Devices, South China University of Technology, Guangzhou, 510640, China*

[3]*Department of Mathematical Sciences, Aalborg University, Aalborg, 9220, Denmark*

[4]*Physics of AmoRphous and Inorganic Solids Laboratory (PARISlab), Department of Civil and Environmental Engineering, University of California, Los Angeles, CA 90095, USA.*

**Corresponding authors. E-mail: taod@bio.aau.dk (T.D.), mos@bio.aau.dk (M.M.S.)*

## Abstract

The first sharp diffraction peak (FSDP) in the reciprocal-space structure factor $S(Q)$ of glasses has been associated with their medium-range order (MRO) structure, but the real-space origin remains debated. While some progress has been made in the case of silicate and borate glasses, the MRO structure of phosphate glasses has not been studied in detail. Here, we apply persistent homology (PH), a topological data analysis method, to extract the MRO features and deconvolute the FSDP of zinc phosphate glasses. To this end, the oxygen, phosphorus, and zinc atoms in the atomic configurations of the glasses are regarded as vertices weighted by initial atom radii for PH computation before decomposing their contributions to the FSDP. To determine the vertex weights, we vary the oxygen (O) radius systematically and set the radii of zinc (Zn) and phosphorus (P) atoms based on the positions of the first peak in the O-Zn and O-P partial radial distribution functions. These configurations with varying atom radii are used as inputs for PH computation, allowing us to assess the contributions of the different ring structures to the MRO. In turn, this comparison between the computed and measured $S(Q)$ gives rise to an optimized oxygen radius for the best agreement. The optimized vertex weight (oxygen radius) is found to have a physical meaning based on the covalent and ionic bonding characters. Finally, using the optimized atom radii, we are able to decompose the hierarchical structural contributions to the FSDP.

**Keywords:** Glass structure; First sharp diffraction peak; Medium-range order; Persistent homology.

## I. INTRODUCTION

Although oxide glasses have found widespread applications [1-3], understanding of their structures remains elusive. This is an important outstanding problem, since glass structure governs the properties and thus the potential applications of the glass [4,5]. While network formers (e.g., $SiO_2$ and $P_2O_5$) in oxide glasses provide the structural backbone, the network modifiers (e.g., $Na_2O$ and CaO) act to charge-stabilize network formers and rupture bridging oxygen bonds [5]. Despite the absence of periodicity and long-range order [6], the glass structure exhibits localized chemical order on the short- and medium-range order (SRO and MRO, respectively) length scales [7]. SRO is defined by the chemical bonds and nearest neighbors of each atom (which can be easily determined by, e.g., nuclear magnetic resonance and diffraction methods), but the MRO beyond the first coordination shell (typically in the range of 5-20 Å) is much more challenging to characterize [8,9]. A typical approach involves neutron or X-ray scattering experiments to measure the structure factor $S(Q)$ [10-12]. Namely, the first sharp diffraction peak (FSDP) of $S(Q)$ is regarded as the characteristic feature related to the MRO structure in glasses. While Elliott interpreted the FSDP of covalent glasses as originating from interstitial volumes around cation-centered structure unit [13], other authors have argued that the FSDP can be ascribed to quasi-Bragg planes [14]. Recently, Ying *et al*. proposed that FSDP originates from real-space ring structures and proposed a method termed RingFSDP to deconvolute the experimental FSDP into various ring structures [15,16]. However, the fundamental fingerprint, particularly the real-space origin of the FSDP still remains an open problem in glass science, mostly because the FSDP is a feature in reciprocal space and the glass structure lacks translational and orientational order [17].

With the development of computational techniques, such as molecular dynamics (MD) simulations and the reverse Monte Carlo method, the atomic configurations in glass can be determined for further structure analysis [18,19]. This has also been enabled by advances in experimental techniques such as atomic resolution imaging using aberration-corrected transmission electron microscopy and atom probe field ion microscopy [20-22]. Such experiments rely on sophisticated facilities involving various corrections and some methods are developed specifically for two-dimensional materials. The simulations therefore offer the advantages of low-cost, easy accessibility, and the possibility to easily perform *in situ* studies. However, simulations provide the entire atomic structure, that is, the position ($x$, $y$, $z$) of each atom—a $3N$-dimensional vector, where $N$ is the number of atoms—which captures all the complexity of glass structure. This complete, high-dimension

representation makes it challenging to isolate the low-dimension structural features that contribute to the first order of the MRO, while filtering out other structural features that only have a second-order contribution. To this end, various tools have been developed, e.g., ring statistics on the bias of covalent bonds [16]. In this work we use the emerging persistent homology (PH) framework to address this challenge.

PH is a method within topological data analysis (TDA) to characterize complex point-cloud data (such as atomic configurations) as input data, with the goal to discern embedded topological features such as clusters (zero-dimensional PH), loops (one-dimensional PH) and voids (two-dimensional PH) [23,24]. PH can provide global and multi-scale topological features with no direct dependence on chemical bonds or dimensions of the materials. While zero-dimensional PH holds similar information as the radial distribution function (RDF), one-dimensional PH holds information on the loop-like structure, which is a typical feature related to the MRO in glasses [25]. Previously, PH has been successfully used to capture the MRO structures and deconvolute the FSDP for different glass systems, such as silica glass [26,27], amorphous ice [28], irradiated hybrid glasses [29], and sodium silicate glasses [25,30]. The atoms in the glasses are treated as vertices and weighted based on the radii of the atoms for the PH computation. The input radii of atoms (vertex weights) have previously been determined by the positions of the first peak in the partial RDFs of $g_{OO}(r)$ and $g_{OM}(r)$ in the case of oxide glass systems, where O and M represent the oxygen and glass former (e.g., Si) or modifier atoms (e.g., Na), respectively [25,26,28]. The oxygen radius ($r_O$) calculated through this method will be larger than the experimental radius of oxygen in the glass because the nearest neighbor of oxygen is M, which could hide some topological features and affect the MRO analysis [31]. In this work, we address the problem of how to determine the optimum radii and hence vertex weights and understand their physical origin within PH. We vary the oxygen (O) radius systematically and set the radii of M atoms based on the positions of the first peak in the O-M partial radial distribution function. These configurations with varying atom radii are used as inputs for PH computation, allowing us to assess the contributions of the different ring structures to the MRO. In turn, this comparison between the computed and measured $S(Q)$ gives rise to an optimized oxygen radius for the best agreement.

To this end, we consider the zinc phosphate ($ZnO\text{-}P_2O_5$; denoted as ZP) glass as a model system and apply weighted PH to study the role of oxygen, as well as zinc and phosphorus in the MRO structure. We note that the phosphate glass system has not yet been studied by the PH method. $P_2O_5$ is a typical network former and

is generally presented as [$PO_4$] tetrahedra, but it differs from the other network formers such as $SiO_2$ by containing a P=O double bond that is shorter than the other three P-O bonds in the [$PO_4$] unit, resulting in electronic delocalization in the phosphate glasses [32]. ZnO can both act as network former and modifier and significantly alter the physical and chemical properties of phosphate glasses [33]. As such, the ZP glass family exhibits unique properties, such as large glass-forming range, low glass transition temperature, excellent durability and high rare earth solubility [34]. This makes ZP glasses promising as sealing materials, optical waveguides, and solid-state laser sources [35,36], but their underlying hierarchical structure remains largely unknown. Here, we generate the atomic configurations of ZP glasses for PH analysis using MD simulations and verify these simulated configurations through comparisons with experimental data on properties and structures. The validated glass configurations are used as input data for PH calculation and we treat the atoms as vertices and vary atom radii systemically to find the optimized weights for PH analysis by calculating a structure factor (which depends on the input radii) and comparing to the validated MD-simulated structure factor. The loops captured utilizing the optimized vertex weights are then used to deconvolute the FSDP of ZP glasses. Notably, we find that the FSDP can be successfully decomposed into MRO loops. Finally, we reveal that the optimized vertex weights for PH computation can be ascribed to the average atom radii weighted by the covalent and ionic bonding characters in the glass.

## II. METHODS

### A. Molecular dynamics simulation

The MD simulations were conducted using the Large-scale Atomic/Molecular Massively Parallel Simulator (LAMMPS) package [37] to reproduce the atomic configurations of ZP glasses with the compositions of $x$ZnO-(100-$x$)$P_2O_5$ ($x$ = 60, 65, 70 mol%; denoted as $x$ZP). These zinc-rich compositions fall between the meta- and ortho-phosphate ones (these glasses are frequently termed polyphosphates). This region not only encompasses the ZP glass that is of commercial interest, but has also proved to be a practical model glass for understanding the structural features of phosphate glasses [38,39]. We utilized the potential proposed by Pedone [40] that has been successfully used to simulate other phosphate glasses [41,42],

$$U(r)=\frac{z_i z_j e^2}{r} + D_{ij}\left[\left\{1-e^{-a_{ij}(r-r_0)}\right\}^2 - 1\right] + \frac{C_{ij}}{r^{12}}. \quad (1)$$

In this potential, the long-range Coulombic interactions above 12 Å are computed using the Particle-Particle Particle-Mesh (PPPM) algorithm with an accuracy of $10^{-5}$. The cutoff of the short-range interaction was set to 15 Å [40], while the simulation timestep was fixed as 1 fs. We applied periodic boundary conditions (PBC) in all directions of the box during the simulations.

We first investigated the effect of system size by simulating 60ZP glasses with different total number of atoms, i.e., 2000, 4000, 6000, 10000, 20000, and 48000 atoms, respectively. As discussed in Section III, a system size of around 10000 atoms achieves a good balance between structural accuracy and computational efficiency. Therefore, around 10000 atoms (10000, 10125, 10150 for 60ZP, 65ZP and 70ZP, respectively) were randomly placed in a cubic box. The systems were then subjected to an energy minimization process with the stopping tolerance for a total force or energy value of $10^{-8}$. Then the temperature was elevated to 6000 K and the system was equilibrated in the *NVT* ensemble for 100 ps to ensure the loss of the memory of its initial configurations. Afterwards, the system was cooled instantaneously to 5000 K, where it was equilibrated for another 45 ps in the *NVT* ensemble, before being quenched from 5000 to 300 K with a cooling rate of 1 K $ps^{-1}$ in the *NPT* ensemble. After the quenching process, the system was further relaxed at 300 K for 45 ps in the *NPT* ensemble. All the simulations were conducted at zero pressure when applicable. The *NPT* simulations were carried out by integration of Nosé-Hoover [43,44] style non-Hamiltonian equations of motion with a barostat damping factor of 1 ps and a thermostat damping factor of 0.1 ps. The thermostat damping factor for *NVT* simulations was also set to 0.1 ps.

**B. Structural characterization**

Based on the generated structures, we then computed the partial RDF $g_{ij}(r)$ as [45],

$$g_{ij}(r) = \frac{\delta n_{ij}(r)}{4\pi r^2 dr \rho_j}, \quad (2)$$

where $\delta n_{ij}(r)$ is the number of particles of type $j$ between distances $r$ and $r + dr$ from a particle of type $i$. $\rho_j = c_j\rho_0$ and $\rho_0 = N/V$ is the average number density of the material (in atoms $Å^{-3}$). $c_i$ and $c_j$ represent the concentration of types $i$ and $j$, respectively. The neutron-weighted total correlation function $T(r)$ was then calculated based on the partial RDF $g_{ij}(r)$ [45],

$$T(r) = 4\pi r\rho_0\left[\sum_{i,j=1}^{n} c_i b_i c_j b_j \left(g_{ij}(r) - 1\right) + \left(\sum_{i=1}^{n} c_i b_i\right)^2\right], \quad (3)$$

where $b_i$, $b_j$ are the bound-coherent-neutron scattering lengths of atom species $i$ and $j$ (5.803, 5.130, and 5.680 fm for oxygen (O), phosphorus (P) and zinc (Zn), respectively) [46]. In addition, $n$ indicates the number of atomic species.

Neutron partial structure factors $S_{ij}(Q)$ of the simulated glasses were calculated on the basis of the Faber-Ziman formalism [45],

$$S_{ij}(Q) = 1 + \rho_0 \int_0^{r_{\max}} 4\pi r^2 (g_{ij}(r) - 1) \frac{\sin(Qr)}{Qr} \frac{\sin(\frac{\pi r}{r_{\max}})}{\frac{\pi r}{r_{\max}}} dr. \quad (4)$$

$Q$ is the wave vector and $r_{\max}$ is the maximum radius for the integration (here half the simulation box size because of the use of PBC). The term $\sin(\pi r/r_{\max})/(\pi r/r_{\max})$ is a Lorch-type function used to reduce ripples of the Fourier transform due to the finite cutoff of $r$. The neutron-weighted total structure factor $S(Q)$ was then calculated from the neutron partial structure factors [45],

$$S(Q) = \sum_{i,j=1}^{n} c_i b_i c_j b_j S_{ij}(Q) / \sum_{i,j=1}^{n} c_i b_i c_j b_j. \quad (5)$$

In addition, we also use the Debye's equation to calculate $S(Q)$ [47],

$$S(Q) = \frac{1}{N} \sum_{i \neq j} b_i b_j \frac{\sin(Q|r_i - r_j|)}{Q|r_i - r_j|}, \quad (6)$$

where $N$ is the total number of atoms in the system studied and $r_j$ is the position of atom $j$.

**C. Persistent homology analyses**

To analyze the MRO structure of ZP glasses, weighted PH is conducted using the libraries of Diode [48] and Dionysus2 [49]. Details of the PH computation are presented in the Supplementary Note 1 and associated Figs. S1-S2 in the Supplemental Material [50]. The MD-simulated atomic configurations of ZP glasses with $N$ atoms centered at $\boldsymbol{x}_i \in \mathbb{R}^3$ ($1 \leq i \leq N$) and a set of input radii, i.e., atomic radii $\boldsymbol{r}_i \in \mathbb{R}$ were used as input data for the PH analysis. First, we replaced the atoms with balls based on the input radii. Then the radii of the balls were increased continuously. A parameter $\alpha$ was introduced to control the radii of the growing balls, where $r_i(\alpha) = \sqrt{r_i^2 + \alpha}$. The "birth" of the $k$th loop was defined as $b_k$ when some growing balls intersected for the first time and formed a closed loop structure at $\alpha_1$ ($b_k = \alpha_1$), and the "death" was defined as $d_k$ when the $k$th loop was filled at $\alpha_2$ ($d_k = \alpha_2$). This can be used to compute the persistence diagram (PD), a plot of birth *vs*. death, which is a useful tool to visualize the PH calculation results. Besides, the persistence (lifetime) of the $k$th loop was defined by the difference of $d_k$ and $b_k$, i.e., $d_k - b_k$. Meanwhile, for each point in the PD, the Dionysus2 software

[49] extracts one loop with corresponding information of birth, death, size (number of atoms) and atomic identifications [51].

The weights, which are determined based on the atomic radii (input radii), are crucial input parameters for the PD computation. Because oxygen is directly coordinated by zinc or phosphorus in ZP glasses, the radii of oxygen ($r_O$), phosphorus ($r_P$), and zinc ($r_{Zn}$) can be estimated as the most probable distance between oxygen and phosphorus (1.51 Å) or zinc (1.96 Å) obtained from the positions of the first peaks in the partial RDFs of $g_{OP}(r)$ and $g_{OZn}(r)$ (see Figs. S3b-S3c in the Supplemental Material [50]),

$$r_O + r_P = 1.51 \text{ Å}, \quad (7)$$

and

$$r_O + r_{Zn} = 1.96 \text{ Å}. \quad (8)$$

The graph of $g_{OO}(r)$ shows that the most probable distance between oxygen and oxygen is 2.48 Å, i.e., $r_O + r_O = 2.48$ Å, as shown in Fig. S3a in the Supplemental Material [50]. The oxygens are further classified into three categories, i.e., the oxygen only coordinated by phosphorus ($O_P$) or zinc ($O_{Zn}$), and the oxygen coordinated by both phosphorus and zinc ($O_{PZn}$). The partial RDFs for the atom pairs of $O_P$-$O_P$, $O_{PZn}$-$O_{PZn}$, and $O_{Zn}$-$O_{Zn}$ illustrate that the most probable distances between these atom pairs are the same, which are equal to 2.48 Å (Fig. S4 in the Supplemental Material [50]). Although these results imply that $r_O$ is likely smaller than 1.24 Å, it is not clear what the determined oxygen radius is due to the fact that the nearest neighbor of oxygen is zinc or phosphorus in ZP glasses. However, based on these results, we assume the radius of $O_P$ and $O_{Zn}$ to be the same for the following PH calculations. Since the bonds of O-P or O-Zn in the glass are a mixture of covalent and ionic characters, the oxygen radius should be larger than its covalent radius (0.66 Å) but smaller than its ionic radius (1.35 Å) [52,53]. To determine the optimum $r_O$ value for the PH computation, we varied $r_O$ from 0.5 Å to 1.3 Å with an interval of 0.025 Å and further varied it from 0.96 Å to 1.04 Å with an interval of 0.01 Å. Correspondingly, $r_P$ and $r_{Zn}$ were calculated using Eqs. (7) and (8). As a result, we obtained 41 PDs for each ZP glass structure. Then, we used the PDs to determine the optimal oxygen radius by comparing the FSDP from the validated total neutron-weighted structure factor $S(Q)$ with that calculated by the function of $S_{PH}(Q)$ based on all the MRO loops [26],

$$S_{\mathrm{PH}}(Q) = \frac{1}{|C_i|}\sum_{(b_k,d_k)\in C_i} \delta\left(Q - \frac{2\pi}{l(d_k)}\right), \quad (9)$$

where $|C_i|$ is the number of elements (loops) of a characteristic region (loop category) $C_i$ in the PD. $\delta$ is the Dirac delta distribution, and $l(d_k) = 2\sqrt{d_k + r^2}$, where $r$ is the input radius of the largest atom in each loop. Afterwards, we used different characteristic regions in the PDs computed by using the optimal oxygen radius to calculate the $S_{PH}(Q)$ functions to deconvolute the contributions of PH loops to the neutron-weighted total structure factor $S(Q)$, particularly the FSDP.

## III. RESULTS AND DISSCUSSION

### A. Validation of simulated ZP glass structures

First, the densities and molar volumes of the simulated ZP glasses are validated by comparing the computational results to the experimental data. As illustrated in Fig. 1a, the density increases while the molar volume (see the molar volume plotted as Fig. S5 in the Supplemental Material [50]) decreases monotonically with increasing ZnO content. We find that the simulated density and molar volume show the same composition dependence as the experimental results [36,54,55] with deviations of less than 5% (see Table S1 in the Supplemental Material [50]).

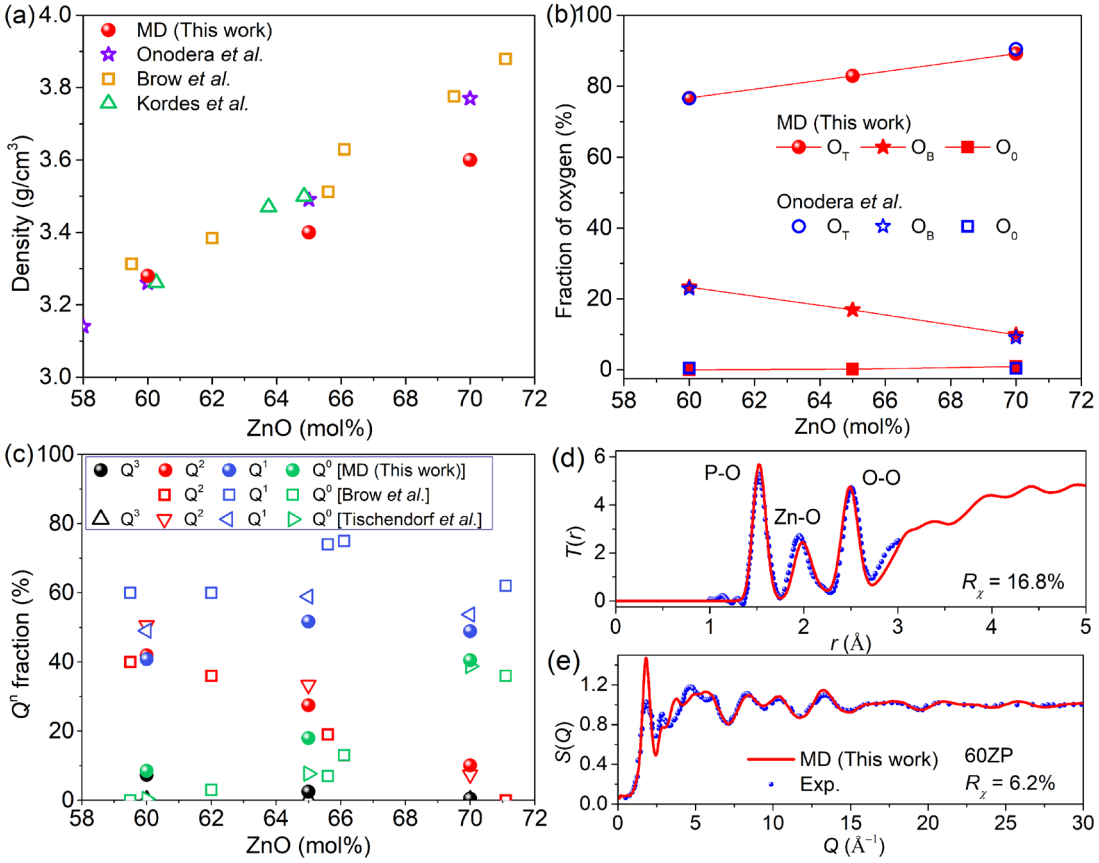


**FIG. 1.** Validation of simulated ZP glasses. Composition dependence of simulated (MD) and experimental (a) density, (b) fractions of oxygen species, and (c) $Q^n$ groups in the ZP glasses. In panel (b), $O_0$, $O_T$ and $O_B$ represent the oxygen free of phosphorus atom, the terminal oxygen (coordinated with 1 phosphorus atom), and the bridging oxygen (coordinated with 2 phosphorus atoms), respectively. Panels (d) and (e) show the comparison of the simulated (MD) and experimental (Exp.) [36] results of the neutron-weighted total correlation function $T(r)$ and the neutron-weighted total structure factor $S(Q)$ for the 60ZP glass, respectively. The $T(r)$ and $S(Q)$ for the 65ZP and 70ZP glasses are shown in Fig. S6 in the Supplemental Material [50].

Next, the structural fingerprints of simulated ZP glasses are compared with experimental data from literatures. The average coordination numbers of phosphorus and zinc atoms in simulated ZP glasses are 4.0 and 4.2, respectively, which agree with the data from refs. [36,56] (see Table S2 in the Supplemental Material [50]). According to the number of neighboring phosphorus around oxygens, the oxygens in ZP glasses are classified as oxygen free of phosphorus $O_0$, terminal oxygen $O_T$ (i.e., coordinated by one phosphorus atom) and bridging oxygen $O_B$ (i.e., coordinated by two phosphorus atoms). The increase of ZnO content increases the O/P ratio, and as a result, the fractions of $O_0$ and $O_T$ increase, while the $O_B$ fraction decreases. These simulated data match well with those reported by Onodera [36] (see Fig. 1b and Table S3 in the Supplemental Material [50]). The $O_B$ content is correlated to the $Q^n$ groups, which is a terminology used to classify the $[PO_4]$

tetrahedra in phosphate glasses. The value of $n$ represents the number of $O_B$ per tetrahedron. As shown in Fig. 1c and Table S4 in the Supplemental Material [50], the fraction of $Q^2$ decreases, while that of $Q^0$ increases as the content of ZnO increases from 60 mol% to 70 mol%. Meanwhile, the fraction of $Q^1$ reaches a maximum value at around 65 mol% ZnO and then drops when the ZnO content further increases. The increase of $Q^1$ might originate from the disproportionation reaction, namely $Q^2 + Q^0 \leftrightarrow 2Q^1$ [32]. Generally, the variation in $Q^n$ groups as a function of ZnO content is well-captured by the simulations when compared with the experimental results [36,54,55].

Figures 1d and 1e display the comparison of experimental and computed neutron-weighted total correlation function $T(r)$ and neutron-weighted total structure factor $S(Q)$ for the 60ZP glass, respectively. $T(r)$ and $S(Q)$ for the 65ZP and 70ZP glasses are shown in Fig. S6 in the Supplemental Material [50]. We note that we do not observe a significant dependence of S($Q$) on the system size (see Fig. S7 in the Supplemental Material [50]). The correlation peaks centered at 1.51, 1.96, and 2.48 Å in $T(r)$ are assigned to the atomic separation distances of P-O, Zn-O, and O-O, respectively. The peak positions and intensities of $T(r)$ show good agreements with the experimental results for both 60ZP and 70ZP glasses [36], indicating that the SRO of the simulated ZP glass is well-reproduced. This is also verified by the excellent agreements between calculated and experimental $S(Q)$ for $Q$ values above 5 Å$^{-1}$. We note that we have calculated $S(Q)$ using both Debye's equation and Fourier transform of the pair distribution function, as shown in Fig. S8 in the Supplemental Material [50]. We find that both methods generate similar $S(Q)$ curves with only minor differences in the intensity of the first diffraction peak. Given the lack of general differences and how the Fourier transformation method generates smoother curves for comparison with PH calculations, we only use the $S(Q)$ calculated by this method in the following analyses.

The $S(Q)$ below 5 Å$^{-1}$ is mainly contributed by MRO structures, and here the positions of the FSDP and second diffraction peak (SDP) in the simulated $S(Q)$ show good agreements with those of the experimental results, indicating that the MRO in ZP glasses is also well-reproduced. The deviations in the intensity of the experimental and calculated $S(Q)$ patterns in the low $Q$ range might be ascribed to the truncation of the Fourier transform at a finite scattering vector $Q$ in reciprocal space, as well as the broadening operations originated from the experiments [57]. In addition, there are likely some inconsistencies between the MD-simulated structure and the real glass structure of glass, for example because the cooling rates available for MD

simulations ($10^9$-$10^{14}$ K/s) are orders of magnitude larger than those in conventional melt-quenching experiments ($10^0$-$10^2$ K/s) [58]. Moreover, we note that the Pedone potential [40] was primarily developed to offer a realistic description of elastic properties (more than structure properties). To quantify the agreements between $S(Q)$ from simulations and experiments, we use the factor $R_\chi$ proposed by Wright [57]. $R_\chi$ values for both 60ZP and 70ZP glass are below 7%. As such, these results generally reveal that the structures of the ZP glasses can be well-reproduced by the MD simulations.

**B. Deconvolution of the $S(Q)$ in the low-$Q$ range**

The validated atomic configurations of the ZP glasses (see the example in Fig. 2a) are used as inputs for the PH computation. The loops captured by PH using Dionysus2 [49] are classified into six mutually exclusive categories (sets) shown as characteristic regions in the PD [25], including $C_S$, $C_3$, $C_4$, $C_5$, $C_6$, and $C_L$ (see Fig. 2b). All the short-range loops, in which all the atoms belong to a [$PO_x$] or a [$ZnO_y$] polyhedron, are classified into $C_S$ firstly. We achieve this by comparing the atomic IDs in each loop extracted by Dionysus2 (denoted as $ID_{loop}$) with the atomic IDs in each [$PO_x$] or [$ZnO_y$] polyhedron captured by the stimulated configurations of ZP glasses (denoted as $ID_{polyhedron}$). A [$PO_x$] or a [$ZnO_y$] polyhedron includes the centered P or Zn atoms as well as the neighboring oxygen atoms in the first shell. They are discerned by using the minimum after the first peak in the partial RDFs with values of 2.0 Å for O-P and 2.6 Å for O-Zn as cutoffs, respectively (Fig. S3 in the Supplemental Material [50]). If the set of $ID_{loop}$ is a subset of one $ID_{polyhedron}$, that loop will be classified into $C_S$. Then the rest of the loops are further sorted into $C_3$, $C_4$, $C_5$, $C_6$, and $C_L$, which contain the loops with 3, 4, 5, 6, and larger than 6 atoms, respectively. The intersection of $C_S \cap C_3 \cap C_4 \cap C_5 \cap C_6 \cap C_L$ is an empty set, namely, each loop only belongs to one category. Note that the birth-death pairs of loops in the PDs are plotted in a squared scale of $Å^2$, which can be correlated to the PH computation operations. To make the PH computation feasible, the union of balls (atoms) is treated as a union of convex shapes to avoid redundant information coming from, e.g., balls (atoms) intersecting when they are already contained in unions of other balls (atoms). This construction works when the weight of a vertex is $\sqrt{r_i^2 + \alpha}$ where $r_i$ is the initial atomic radius. This means that the unit of the increment alpha ($\alpha$) is in length squared [25].

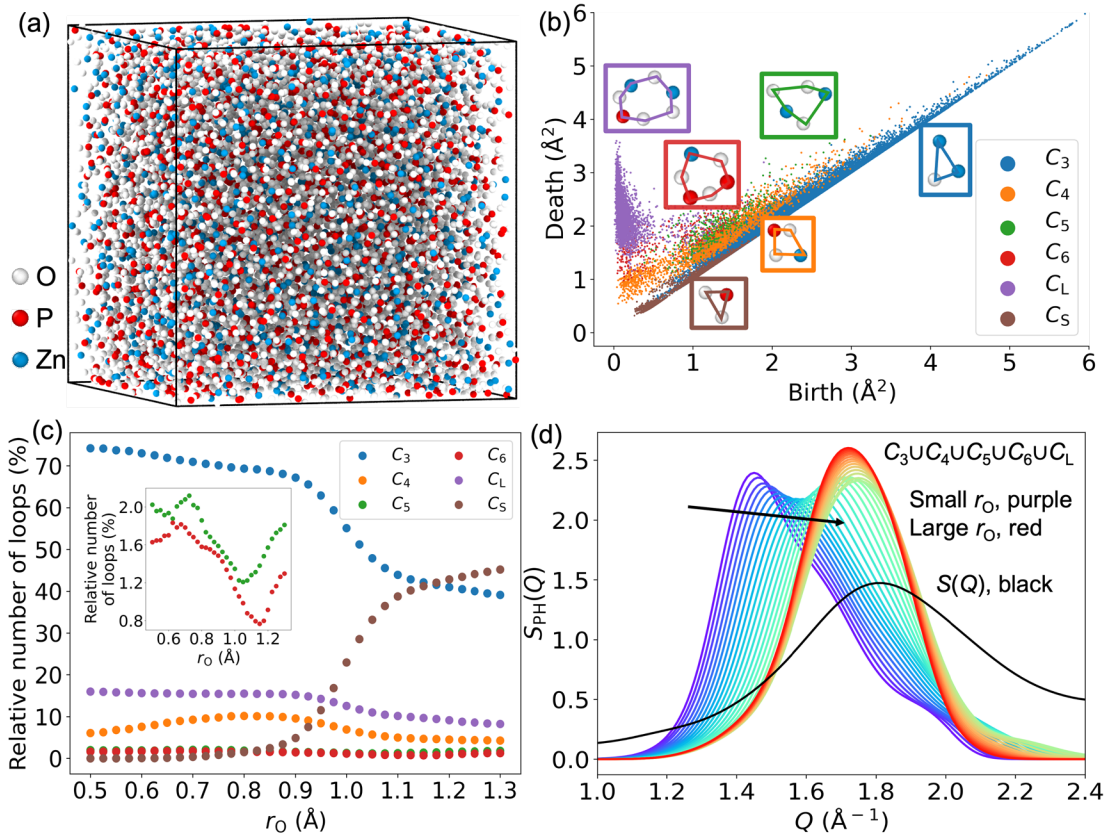


**FIG. 2.** Schematic overview of input radii optimization and dimension one persistent homology analysis. (a) Atomic configuration of 60ZP glass at 300 K, which is used as input data for the PH calculation. (b) A PD of 60ZP glass with colored characteristic regions related to the loop categories, along with example loop structures for each loop category. (c) Dependence of the relative number of loops in each category on $r_O$ with an interval of 0.025 Å for the 60ZP glass. (d) $S_{PH}(Q)$ calculated by the union of $C_3 \cup C_4 \cup C_5 \cup C_6 \cup C_L$ for the 60ZP glass with varying $r_O$ from 0.5 Å to 1.3 Å.

Figure 2b illustrates a PD of 60ZP glass with colored characteristic regions corresponding to the loop categories along with example loop structures for each loop category. Besides, we note that we do not observe a significant dependence of the PD features on the system size (see Figs. S9-S10 in the Supplemental Material [50]). As observed in Fig. 2b, the loops in $C_S$ and $C_3$ (most are three-membered loops) are distributed close to the PD diagonal, while the large loops ($C_L$) are located vertically at the low-birth region. The birth of a loop mainly relies on the distance of neighboring atoms, while the death is dominated by the longest distance between the atoms in the loop. The three-membered loops (triangles) are mainly formed by the neighboring atoms in the localized structure, resulting in a relatively short lifetime. The large loops are composed of

medium-range interacting atoms and atoms which are far apart, and therefore, they can persist for a longer lifetime.

Calculated PDs of the ZP glasses with selected starting oxygen radii ($r_O$) are shown in Figs. S11-S13 in the Supplemental Material [50]. As can be seen, the total number of brown points, i.e., loops belonging to the $C_S$, as well as the area of $C_S$ region in the PDs, increases significantly with rising $r_O$. Dependence of the loop fractions (in %) for each category on $r_O$ of the 60ZP glass is further computed and presented in Fig 2c. Corresponding results of 65ZP and 70ZP glasses are illustrated in Fig. S14 in the Supplemental Material [50]. The total fraction of loops in $C_3$ and $C_S$ is larger than 70%. The number of loops ($N_{loop}$) in $C_S$ increases by 2% as $r_O$ increases from 0.5 Å to 0.9 Å, and rises to 40% when $r_O$ increases from 0.9 Å to 1.1 Å. Then, it increases further to ~48% as $r_O$ increases from 1.1 Å to 1.3 Å. Furthermore, $N_{loop}$ in $C_3 \cup C_4 \cup C_5 \cup C_6 \cup C_L \cup C_S$ (Fig. S15a in the Supplemental Material [50]) shows a comparable trend when $r_O$ increases with that in $C_S$ (Fig. S15c in the Supplemental Material [50]). However, $N_{loop}$ in the union of $C_3 \cup C_4 \cup C_5 \cup C_6 \cup C_L$ increases by about 5% when $r_O$ increases to 0.65 Å and decreases by around 12% as $r_O$ further increases to 1.3 Å (Fig. S15b in the Supplemental Material [50]). This result demonstrates that the increase of $r_O$ leads to an increase of loops belonging to $C_S$. As $r_O$ increases, the distance between spherical (atomic) surfaces of neighboring oxygen atoms decreases (see Fig. S16 in the Supplemental Material [50]). Consequently, the neighboring oxygen atoms have an increased probability to first intersect with each other and the neighboring phosphorus or zinc atoms. This will give rise to $C_S$ when the radii of all the atoms increase synchronously during the PH calculation.

To determine the optimum value of $r_O$, we compute the $S_{PH}(Q)$ function for the union of $C_3 \cup C_4 \cup C_5 \cup C_6 \cup C_L$ at all studied values of $r_O$. These results are presented in Fig. 2d and Figs. S17-S18 in the Supplemental Material [50]. $C_S$ is neglected in this analysis since these loops, per definition, originate from SRO, while the FSDP represents MRO. We find that $S_{PH}(Q)$ is highly sensitive to the value of $r_O$. Dependence of corresponding peak position of $S_{PH}(Q)$ on $r_O$ is shown in Fig. S19 in the Supplemental Material [50]. As $r_O$ increases, the peak position of $S_{PH}(Q)$ increases to a maximum value around 1.75 Å$^{-1}$ when $r_O$ reaches 0.97 Å - 1.02 Å, showing the best agreement to the peak position of FSDP in $S(Q)$ calculated by the MD-simulated glass configurations (1.80 Å$^{-1}$ for 60ZP, 1.82 Å$^{-1}$ for 65ZP, and 1.86 Å$^{-1}$ for 70ZP). When $r_O$ further increases, the peak position of $S_{PH}(Q)$ decreases slightly. The partial $S_{PH}(Q)$ calculated by the loop categories of $C_3$, $C_4$, $C_5$, $C_6$, $C_L$ and $C_S$ also depend on $r_O$, as shown in Figs. S20-S22 in the Supplemental Material [50]. That is, their peak positions also

increase to a maximum value as $r_O$ increases to around 1 Å, which are followed by a slight decrease when $r_O$ further increases. The dependence of the peak position of the partial $S_{PH}(Q)$ on $r_O$ shows a similar tendency compared to that of the $S_{PH}(Q)$ calculated by the union of $C_3 \cup C_4 \cup C_5 \cup C_6 \cup C_L$.

We now use the factor $R_\chi$ proposed by Wright [57] to quantify the general agreement between $S_{PH}(Q)$ and $S(Q)$. The intensities of $S(Q)$ and $S_{PH}(Q)$ are normalized from zero to one before calculating the $R_\chi$. As shown in Fig. S23 in the Supplemental Material [50], $R_\chi$ of $S_{PH}(Q)$ and $S(Q)$ reaches a minimum value when $r_O$ is 0.98 Å, corresponding to the best agreement between $S_{PH}(Q)$ and $S(Q)$ when using this value as oxygen radius (weight) for the PH calculation. Hence, the PDs calculated using a value of $r_O$ of 0.98 Å (see Figs. S11c, S12c and S13c in the Supplemental Material [50]) are employed for further analysis. We note that we simply use the factor $R_\chi$ to find the optimum $r_O$. Indeed, the intensities of $S_{PH}(Q)$ and $S(Q)$ are not comparable, but their shapes and peak positions can be correlated. The $S_{PH}(Q)$ is calculated based on the kernel density estimation algorithm of the manually defined loop parameters ($\frac{2\pi}{l(d_k)}$), which is normalized by the number of loops in related loop category (Eq. 9). $S_{PH}(Q)$ reflects the contributions (relative intensities) of different loop categories at various $Q$ value, while $S(Q)$ (Eq. 5) is the summation of the partial neutron structure factors, $S_{ij}(Q)$ (Eq. 4), calculated from the Fourier transform of related partial radial distribution function $g_{ij}(r)$ (Eq. 2).

The loops extracted by the PH analysis might be MRO structural descriptors that are responsible for the FSDP in $S(Q)$ [25,26,30]. Therefore, we compare the $S_{PH}(Q)$ calculated by using the characteristic regions of $C_3$, $C_4$, $C_5$, $C_6$, and $C_L$ as well as their union and the structure factor $S(Q)$ around the FSDP, as shown in Fig. 3 and Fig. S24 in the Supplemental Material [50]. The $S_{PH}(Q)$s for 60ZP glass with different system sizes are also provided in Figs. S25-S26 in the Supplemental Material [50], revealing that a system size of 10000 atoms offers sufficient statistics. As shown in Fig. 3, the $S_{PH}(Q)$ computed by the union of $C_3 \cup C_4 \cup C_5 \cup C_6 \cup C_L$ shows excellent agreement in terms of peak position (1.75 $Å^{-1}$) and plot shape compared with those of $S(Q)$ (1.80 $Å^{-1}$). The $C_3$ and $C_L$ contribute to the lowest $Q$ range, the $C_5$ contributes to the medium $Q$ range, and the $C_4$ and $C_6$ contribute to the highest $Q$ range of FSDP. This implies that FSDP can be ascribed to the medium-range loops in the glass.

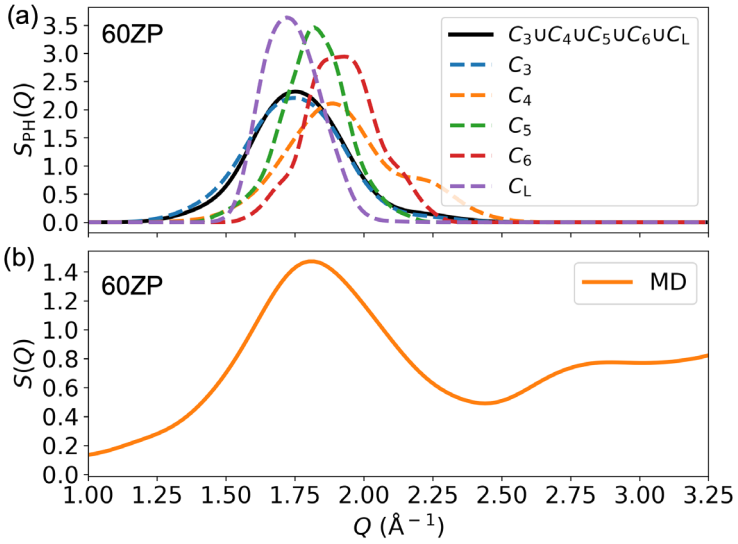


**FIG. 3.** Deconvolution of the FSDP. Comparison between the (a) $S_{PH}(Q)$ calculated by the characteristic regions of $C_3$, $C_4$, $C_5$, $C_6$, and $C_L$ as well as their union and (b) structure factor $S(Q)$. Both are shown for the 60ZP glass. Corresponding results for 65ZP and 70ZP glasses are shown in Fig. S24 in the Supplemental Material [50]. We note that the absolute values on the two y-axes are not directly comparable as discussed in the text.

To further understand the composition dependence of the contributions of various characteristic regions in PD to the FSDP, the structure factor $S(Q)$ and the functions of $S_{PH}(Q)$ of $C_3$, $C_4$, $C_5$, $C_6$, and $C_L$ as well as their union have been calculated for all the simulated ZP glasses (Fig. 4). We find that the peak position of $S_{PH}(Q)$ function for the union of $C_3 \cup C_4 \cup C_5 \cup C_6 \cup C_L$ shifts to a higher $Q$ value as the ZnO concentration increases (Fig. 4a). This is in agreement with the tendency of the $S(Q)$ as a function of ZnO content (Fig. 4b). Furthermore, the peak positions of $S_{PH}(Q)$ for $C_5$, $C_6$, and $C_L$ increase significantly, while that of $C_3$ shows few changes and that of $C_4$ decreases slightly with increasing content of ZnO. These results reveal that the shifts in FSDP are dominated by loops with more than four atoms. Moreover, the shoulder peak at about 2.23 Å$^{-1}$ in the $S_{PH}(Q)$ function for the union of $C_3 \cup C_4 \cup C_5 \cup C_6 \cup C_L$ (Fig. 4a) can be correlated to the shoulder peak of $S_{PH}(Q)$ for $C_4$ (Fig. 4d).

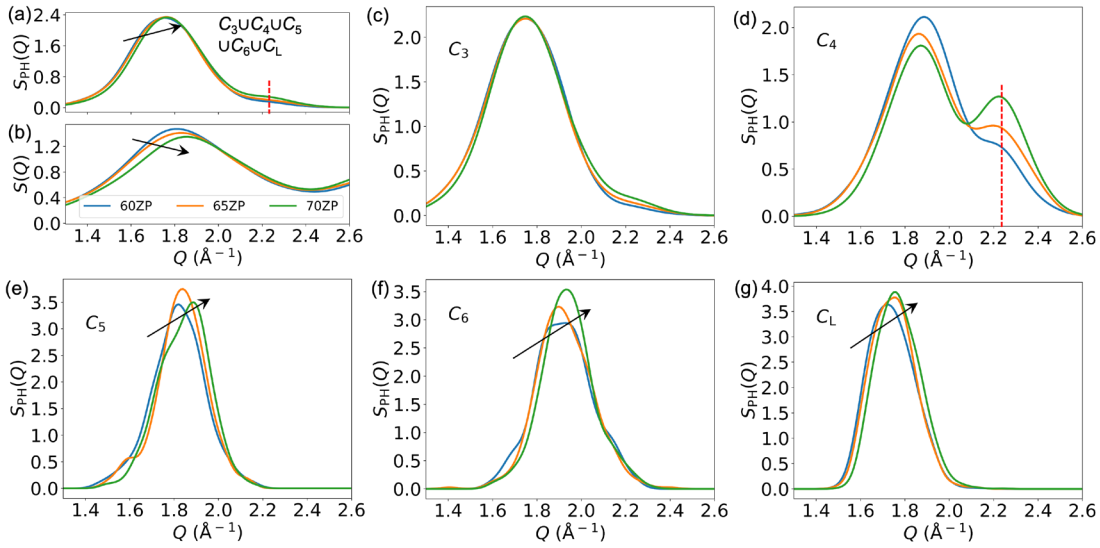


**FIG. 4.** Composition dependence of the contributions of various characteristic regions in the PD to the FSDP. A comparison between $S_{PH}(Q)$ computed from (a) the union of $C_3 \cup C_4 \cup C_5 \cup C_6 \cup C_L$, (c) $C_3$, (d) $C_4$, (e) $C_5$, (f) $C_6$ and (g) $C_L$ of PD, and (b) $S(Q)$ computed using the RDFs of MD-simulated atomic configurations. All color coding is the same as in Fig. 4b. Arrows indicate peak shifting tendency with increasing ZnO content.

Finally, we analyze the contributions of the short-range loops, $C_S$, to the structure factor $S(Q)$ of ZP glasses (Fig. 5). The results demonstrate that $C_S$ contains only three-membered loops with two oxygens and one zinc or one phosphorus when the input radius (weight) of oxygen is 0.98 Å for PH calculation (see Fig. S27 in the Supplemental Material [50]). Figure 5 presents the comparison of $S_{PH}(Q)$ calculated by $C_S$ and structure factor $S(Q)$ ranging from 1 Å$^{-1}$ to 3.25 Å$^{-1}$. The $S_{PH}(Q)$ calculated by $C_S$ shows two distinct peaks centered at around 2.2 Å$^{-1}$ and 2.6 Å$^{-1}$, which are comparable to the positions of the FSDP at higher $Q$ range and the second diffraction peak (SDP) in $S(Q)$, respectively. Besides, the relative intensity of the peak centered at 2.6 Å$^{-1}$ in $S_{PH}(Q)$ is about four times as strong as that at 2.2 Å$^{-1}$. These results suggest that the region $C_S$ also contributes to the intensity of the FSDP at around 2.2 Å$^{-1}$, but more importantly, the SDP for the ZP glass can be decomposed into the short-range structures within the [$PO_x$] and [$ZnO_y$] polyhedra. Recently, Rui and Tanaka proposed a "tetrahedron model" to explain the FSDP of covalent tetrahedral liquids and glasses, such as amorphous $SiO_2$, based on the formation of locally favored tetrahedral structure ([$SiO_4$]) [59]. Our study reveals that the [$PO_x$] and [$ZnO_y$] units in the ZP glasses contribute partially to the FSDP at higher $Q$ range (around 2.2 Å$^{-1}$) but mainly contribute to the SDP in the structure factor $S(Q)$. This might be ascribed to the presence of mixed covalent and ionic bonds in the ZP glasses.

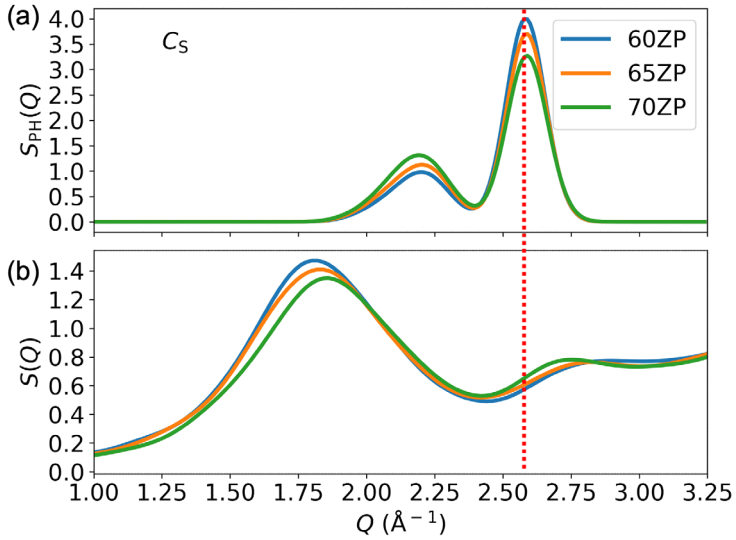


**FIG. 5.** Contribution of $C_S$ to the structure factor $S(Q)$. (a) $S_{PH}(Q)$ calculated by $C_S$ and (b) $S(Q)$ calculated by the MD-simulated structure.

### C. Physical origin of optimized $r_O$ value

Based on the PH analysis, we have obtained an optimum weight (radius) for the oxygen atom of $r_O$ = 0.98 Å in the ZP glasses from the mathematical operations, yet without a clear physical interpretation of this optimum. Therefore, in the following, we address the underlying physical meaning of this optimized $r_O$ value. We note that although the optimum radius of oxygen is an averaged value of different local environments, the slightly different values of oxygen radius do not influence the PH calculations. This is confirmed by considering the local anisotropy of oxygen for PH calculations, as shown in Fig. S28 in the Supplemental Material [50]. That is, the averaged oxygen radius used in this study can capture the structure features when applying the PH method.

Generally, the oxygen atoms in ZP glasses interact with the phosphorus or zinc atoms through mostly covalent bonds and ionic bonds, respectively. From this standpoint it is thus meaningful to suggest that the radius of oxygen in the glass could depend on the covalent and ionic characters between oxygen and phosphorus or zinc. To this end, we define a quantitative parameter, $\overline{r_O}$, as the average radius for oxygen, which is computed by the summation of the covalent radius of oxygen weighted by its covalency fraction, and the ionic radius of oxygen weighted by its ionicity fraction on the basis of the glass configuration,

$$\overline{r_O} = \frac{[f_{OP}\times r_{O\_ion}+(1-f_{OP})\times r_{O\_cov}]\times N_{OP}+[f_{OZn}\times r_{O\_ion}+(1-f_{OZn})\times r_{O\_cov}]\times N_{OZn}}{N_{OP}+N_{OZn}}. \quad (10)$$

Here, $r_{\mathrm{O\_ion}}$ and $r_{\mathrm{O\_cov}}$ are the ionic radius and covalent radius of oxygen, respectively, and $N_{\mathrm{OP}}$ and $N_{\mathrm{OZn}}$ are the number of bonds between oxygen and phosphorus and oxygen and zinc, respectively, in the MD-simulated ZP glasses. The term "bond" is here counted when the distance between oxygen and phosphorus, or oxygen and zinc is less than the minimum after the first peak in the partial RDFs of O-P (2.0 Å) and O-Zn (2.6 Å), respectively (Fig. S3 in the Supplemental Material [50]). The factors, $f_{\mathrm{OP}}$ and $f_{\mathrm{OZn}}$, represent the fractional ionic character of the bonds between oxygen and phosphorus and oxygen and zinc, respectively. The fractional ionic character $f_{\mathrm{AB}}$ of two elements A and B is calculated according to Pauling's algorithms by [60],

$$f_{\mathrm{AB}} = 1 - \exp\left[-\frac{1}{4}(\chi_{\mathrm{A}} - \chi_{\mathrm{B}})^2\right], \qquad (11)$$

where $(\chi_{\mathrm{A}} - \chi_{\mathrm{B}})$ is a measure of the electronegativity difference between the elements A and B.

The calculated average radius of oxygen $\overline{r_{\mathrm{O}}}$ for the ZP glasses is listed in Table 1. The $\overline{r_{\mathrm{O}}}$ value of around 0.96 Å is in excellent agreement with the optimized input radius of oxygen $r_{\mathrm{O}}$ (0.98 Å) obtained by the PH analysis. This small difference (<3%) indicates that the optimized weights for the PH computation can be correlated to the covalency and ionicity weighted average radius of the atoms in the studied glass materials. As such, the $\overline{r_{\mathrm{O}}}$ parameters could also be used for determining the optimum input atom radius for PH and the weighted PH method can provide a better understanding of glass structure on the basis of atomic radii. Our study therefore highlights the importance of optimizing the vertex weights (input atomic radii) for PH computation to understand the structure of glasses and other material families. In particular, it would be interesting in future work to also perform PH analyses in covalently bonded chalcogenide glasses, which might allow for a simpler interpretation of the FSDP.

**TABLE 1.** Pauling electronegativity $\chi$, ionic radius $r_{\mathrm{ion}}$, covalent radius $r_{\mathrm{cov}}$, and calculated average radius of oxygen $\overline{r_{\mathrm{O}}}$ in ZP glasses.

| Element | $\chi$ [61] | $r_{\mathrm{ion}}$ (Å) [53] | $r_{\mathrm{cov}}$ (Å) [52] | $\overline{r_{\mathrm{O}}}$ (Å) |
|---|---|---|---|---|
| O | 3.44 | 1.35 | 0.66 | 0.95 (60ZP) |
| P | 2.19 | 0.17 | 1.07 | 0.96 (65ZP) |
| Zn | 1.65 | 0.60 | 1.22 | 0.97 (70ZP) |

## IV. CONCLUSIONS

We have used weighted persistent homology (PH) to analyze the medium-range order structure of zinc phosphate glasses and decipher the real-space origin of their structure factor $S(Q)$ at $Q < 3.25$ Å$^{-1}$, which includes the first sharp diffraction peak (FSDP) and second diffraction peak (SDP). By systemically varying the input weights (radii) of the atoms, we find an optimum vertex weight (oxygen radius) for PH computation to extract the loop structures and deconvolute the $S(Q)$. The results reveal that the signal of FSDP at around 1.8 Å$^{-1}$ is dominated by the loops with the size larger than four, while the signal intensity at around 2.2 Å$^{-1}$ is mainly contributed by the loops with the small sizes of three and four. The SDP at around 2.60 Å$^{-1}$ can be ascribed to the short-rang loops associated with [$PO_x$] or [$ZnO_y$] polyhedra. Furthermore, the optimized atomic radius of oxygen can be correlated to the physical meaning of average oxygen radius weighted by its ionic and covalent characters in the glass. This work not only offers a deeper physical insight into the MRO structure of oxide glasses, but also paves a way on how to optimize vertex wights (atom radii) for persistent homology when using to understand the structure of disordered materials as described by complex point-cloud data.


## ACKNOWLEDGEMENTS

This work is jointly supported by China Scholarship Council (CSC No. 202106150038), Marie Skłodowska-Curie Individual Fellowship (101018156), and Independent Research Fund Denmark (1026-00037). M.B. acknowledges funding from the National Science Foundation under grant DMR-1944510.


## NOTES

The authors declare no competing interests.

## REFERENCES


[1] K. Sun, D. Tan, X. Fang, X. Xia, D. Lin, J. Song, Y. Lin, Z. Liu, M. Gu, Y. Yue, and J. Qiu, *Three-dimensional direct lithography of stable perovskite nanocrystals in glass*, Science **375**, 307 (2022).

[2] P. H. Abelson, *Glass fiber communication*, Science **220**, 463 (1983).

[3] R. Dylla-Spears, T. D. Yee, K. Sasan, D. T. Nguyen, N. A. Dudukovic, J. M. Ortega, M. A. Johnson, O. D. Herrera, F. J. Ryerson, and L. L. Wong, *3D printed gradient index glass optics*, Sci. Adv. **6**, eabc7429 (2020).

[4] Q. Y. Zhang, W. J. Zhang, W. C. Wang, and Z. H. Jiang, *Calculation of physical properties of glass via the phase diagram approach*, J. Non-Cryst. Solids **457**, 36 (2017).

[5] Z. H. Jiang and Q. Y. Zhang, *The structure of glass: A phase equilibrium diagram approach*, Prog. Mater. Sci. **61**, 144 (2014).

[6] W. H. Zachariasen, *The atomic arrangement in glass*, J. Am. Chem. Soc. **54**, 3841 (1932).
[7] J. W. E. Drewitt, L. Hennet, and D. R. Neuville, *From short to medium range order in glasses and melts by diffraction and raman spectroscopy*, Rev. Mineral Geochem. **87**, 55 (2022).
[8] M. Edén, *NMR studies of oxide-based glasses*, Annu. Rep. Prog. Chem., Sect. C: Phys. Chem. **108**, 177 (2012).
[9] S. R. Elliott, *Medium-range structural order in covalent amorphous solids*, Nature **354**, 445 (1991).
[10] U. Hoppe, R. Kranold, A. Barz, D. Stachel, J. Neuefeind, and D. A. Keen, *Combined neutron and X-ray scattering study of phosphate glasses*, J. Non-Cryst. Solids **293-295**, 158 (2001).
[11] P. H. Gaskell, *Medium-range structure in glasses and low-Q structure in neutron and X-ray scattering data*, J. Non-Cryst. Solids **351**, 1003 (2005).
[12] P. H. Gaskell, M. C. Eckersley, A. C. Barnes, and P. Chieux, *Medium-range order in the cation distribution of a calcium silicate glass*, Nature **350**, 675 (1991).
[13] S. R. Elliott, *Origin of the first sharp diffraction peak in the structure factor of covalent glasses*, Phys. Rev. Lett. **67**, 711 (1991).
[14] P. H. Gaskell and D. J. Wallis, *Medium-range order in silica, the canonical network glass*, Phys. Rev. Lett. **76**, 66 (1996).
[15] Y. Shi, J. Neuefeind, D. Ma, K. Page, L. A. Lamberson, N. J. Smith, A. Tandia, and A. P. Song, *Ring size distribution in silicate glasses revealed by neutron scattering first sharp diffraction peak analysis*, J. Non-Cryst. Solids **516**, 71 (2019).
[16] Q. Zhou, Y. Shi, B. Deng, J. Neuefeind, and M. Bauchy, *Experimental method to quantify the ring size distribution in silicate glasses and simulation validation thereof*, Sci. Adv. **7**, eabh1761 (2021).
[17] T. Uchino, J. D. Harrop, S. N. Taraskin, and S. R. Elliott, *Real and reciprocal space structural correlations contributing to the first sharp diffraction peak in silica glass*, Phy. Rev. B **71**, 014202 (2005).
[18] D. A. Keen and R. L. McGreevy, *Structural modelling of glasses using reverse Monte Carlo simulation*, Nature **344**, 423 (1990).
[19] C. Massobrio, J. Du, M. Bernasconi, and P. S. Salmon, *Molecular Dynamics Simulations of Disordered Materials* (Springer Cham, 2015), Springer Series in Materials Science.
[20] Y. Yang, J. Zhou, F. Zhu, Y. Yuan, D. J. Chang, D. S. Kim, M. Pham, A. Rana, X. Tian, Y. Yao, S. J. Osher, A. K. Schmid, L. Hu, P. Ercius, and J. Miao, *Determining the three-dimensional atomic structure of an amorphous solid*, Nature **592**, 60 (2021).
[21] B. Gault, A. Chiaramonti, O. Cojocaru-Mirédin, P. Stender, R. Dubosq, C. Freysoldt, S. K. Makineni, T. Li, M. Moody, and J. M. Cairney, *Atom probe tomography*, Nat. Rev. Methods Prim **1**, 51 (2021).
[22] P. Y. Huang, S. Kurasch, J. S. Alden, A. Shekhawat, A. A. Alemi, P. L. McEuen, J. P. Sethna, U. Kaiser, and D. A. Muller, *Imaging atomic rearrangements in two-dimensional silica glass: watching silica's dance*, Science **342**, 224 (2013).
[23] T. Ichinomiya, I. Obayashi, and Y. Hiraoka, *Persistent homology analysis of craze formation*, Phys. Rev. E **95**, 012504 (2017).
[24] A. Zomorodian and G. Carlsson, *Computing persistent homology*, Discrete. Comput. Geom. **33**, 249 (2005).
[25] S. S. Sørensen, C. A. N. Biscio, M. Bauchy, L. Fajstrup, and M. M. Smedskjaer, *Revealing hidden medium-range order in amorphous materials using topological data analysis*, Sci. Adv. **6**, eabc2320 (2020).
[26] Y. Hiraoka, T. Nakamura, A. Hirata, E. G. Escolar, K. Matsue, and Y. Nishiura, *Hierarchical structures of*

*amorphous solids characterized by persistent homology*, Proc. Natl. Acad. Sci. **113**, 7035 (2016).

[27] M. Murakami, S. Kohara, N. Kitamura, J. Akola, H. Inoue, A. Hirata, Y. Hiraoka, Y. Onodera, I. Obayashi, J. Kalikka, N. Hirao, T. Musso, A. S. Foster, Y. Idemoto, O. Sakata, and Y. Ohishi, *Ultrahigh-pressure form of $SiO_2$ glass with dense pyrite-type crystalline homology*, Phy. Rev. B **99**, 045153 (2019).

[28] S. Hong and D. Kim, *Medium-range order in amorphous ices revealed by persistent homology*, J. Phys.: Condens. Matter **31**, 455403 (2019).

[29] T. Du, S. S. Sørensen, Q. Zhou, M. Bauchy, and M. M. Smedskjaer, *Accessing a Forbidden Disordered State of a Zeolitic Imidazolate Framework with Higher Stiffness and Toughness through Irradiation*, Chem. Mater. **34**, 8749 (2022).

[30] S. S. Sørensen, T. Du, C. A. N. Biscio, L. Fajstrup, and M. M. Smedskjaer, *Persistent homology: A tool to understand medium-range order glass structure*, Journal of Non-Crystalline Solids: X, 100123 (2022).

[31] Z. Meng, D. V. Anand, Y. Lu, J. Wu, and K. Xia, *Weighted persistent homology for biomolecular data analysis*, Sci. Rep. **10**, 2079 (2020).

[32] R. K. Brow, *Review: the structure of simple phosphate glasses*, J. Non-Cryst. Solids **263**, 1 (2000).

[33] H. Takebe, Y. Baba, and M. Kuwabara, *Dissolution behavior of $ZnO–P_2O_5$ glasses in water*, J. Non-Cryst. Solids **352**, 3088 (2006).

[34] B. C. Tischendorf, T. M. Alam, R. T. Cygan, and J. U. Otaigbe, *The structure and properties of binary zinc phosphate glasses studied by molecular dynamics simulations*, J. Non-Cryst. Solids **316**, 261 (2003).

[35] B. Tischendorf, J. U. Otaigbe, J. W. Wiench, M. Pruski, and B. C. Sales, *A study of short and intermediate range order in zinc phosphate glasses*, J. Non-Cryst. Solids **282**, 147 (2001).

[36] Y. Onodera, S. Kohara, H. Masai, A. Koreeda, S. Okamura, and T. Ohkubo, *Formation of metallic cation-oxygen network for anomalous thermal expansion coefficients in binary phosphate glass*, Nat. Commun. **8**, 15449 (2017).

[37]S. Plimpton, *Fast parallel algorithms for short-range molecular dynamics*, J. Comput. Phys. **117**, 1 (1995).

[38] S. Kapoor, N. Lönnroth, R. E. Youngman, S. J. Rzoska, M. Bockowski, L. R. Jensen, and M. M. Smedskjaer, *Pressure-driven structural depolymerization of zinc phosphate glass*, J. Non-Cryst. Solids **469**, 31 (2017).

[39] B. C. Sales, J. U. Otaigbe, G. H. Beall, L. A. Boatner, and J. O. Ramey, *Structure of zinc polyphosphate glasses*, J. Non-Cryst. Solids **226**, 287 (1998).

[40] A. Pedone, G. Malavasi, M. C. Menziani, A. N. Cormack, and U. Segre, *A new self-consistent empirical interatomic potential model for oxides, silicates, and silica-based glasses*, J. Phys. Chem. B **110**, 11780 (2006).

[41] G. Broglia, C. Mugoni, C. Siligardi, and M. Montorsi, *Lithium and copper transport properties in phosphate glasses: A Molecular Dynamics study*, J. Non-Cryst. Solids **481**, 522 (2018).

[42] G. Broglia, C. Mugoni, J. Du, C. Siligardi, and M. Montorsi, *Lithium vanado-phosphate glasses: Structure and dynamics properties studied by molecular dynamics simulations*, J. Non-Cryst. Solids **403**, 53 (2014).

[43] W. G. Hoover, *Canonical dynamics: Equilibrium phase-space distributions*, Phys. Rev. A. **31**, 1695 (1985).

[44] S. Nosé, *A molecular dynamics method for simulations in the canonical ensemble*, Mol. Phys. **52**, 255 (1984).

[45] D. A. Keen, *A comparison of various commonly used correlation functions for describing total scattering*, J. Appl. Crystallogr. **34**, 172 (2001).

[46] V. F. Sears, *Neutron scattering lengths and cross sections*, Neutron News **3**, 26 (1992).

[47] https://isaacs.sourceforge.net/phys/scatt.html.
[48] Diode—Persistent homology software; https://github.com/mrzv/diode/.
[49] Dionysus2—Persistent homology software; https://mrzv.org/software/dionysus2/.
[50] See Supplemental Material at http://XXXXXXXXX for further details about persistent homology computation, density and structure data, partial radial distribution functions, neutron-weighted total correlation function and total structure factor, persistence diagrams, fractions of loops, computed structure factor, FSDP peak position, and deconvolution of FSDP.
[51] C. A. N. Biscio and J. Møller, *The Accumulated Persistence Function, a New Useful Functional Summary Statistic for Topological Data Analysis, With a View to Brain Artery Trees and Spatial Point Process Applications*, J. Comput. Graph. Stat. **28**, 671 (2019).
[52] B. Cordero, V. Gómez, A. E. Platero-Prats, M. Revés, J. Echeverría, E. Cremades, F. Barragán, and S. Alvarez, *Covalent radii revisited*, Dalton Trans., 2832 (2008).
[53] R. D. Shannon, *Revised effective ionic radii and systematic studies of interatomic distances in halides and chalcogenides*, Acta Crystallogr. A **32**, 751 (1976).
[54] R. K. Brow, D. R. Tallant, S. T. Myers, and C. C. Phifer, *The short-range structure of zinc polyphosphate glass*, J. Non-Cryst. Solids **191**, 45 (1995).
[55] E. Kordes, *Physikalisch-chemische untersuchungen über den feinbau von gläsern*, Z. Phys. Chem. **50**, 194 (1941).
[56] K. Suzuya, K. Itoh, A. Kajinami, and C. K. Loong, *The structure of binary zinc phosphate glasses*, J. Non-Cryst. Solids **345**, 80 (2004).
[57] A. C. Wright, *The comparison of molecular dynamics simulations with diffraction experiments*, J. Non-Cryst. Solids **159**, 264 (1993).
[58] H. Liu, Z. Zhao, Q. Zhou, R. Chen, K. Yang, Z. Wang, L. Tang, and M. Bauchy, *Challenges and opportunities in atomistic simulations of glasses: a review*, Comptes Rendus. Géoscience **354**, 1 (2022).
[59] R. Shi and H. Tanaka, *Distinct signature of local tetrahedral ordering in the scattering function of covalent liquids and glasses*, Sci. Adv. **5**, eaav3194 (2019).
[60] M. Lenglet, *Iono-covalent character of the metal–oxygen bonds in oxides: a comparison of experimental and theoretical data*, Act. Passiv. Electron. Compon. **27**, 1 (2004).
[61] A. L. Allred, *Electronegativity values from thermochemical data*, J. Inorg. Nucl. Chem. **17**, 215 (1961).